

# Adaptive-basis sample-based neural diagonalization for quantum many-body systems

Simone Cantori<sup>1,2\*</sup>, Luca Brodolini<sup>1,2</sup>, Edoardo Recchi<sup>1</sup>, Emanuele Costa<sup>3,4</sup>, Bruno Juliá-Díaz<sup>3,4</sup> and Sebastiano Pilati<sup>1,2</sup>

<sup>1</sup> School of Science and Technology, Physics Division, University of Camerino, I-62032 Camerino (MC), Italy

<sup>2</sup> INFN-Sezione di Perugia, 06123 Perugia, Italy

<sup>3</sup> Departament de Física Quàntica i Astrofísica, Facultat de Física, Universitat de Barcelona, 08028 Barcelona, Spain

<sup>4</sup> Institut de Ciències del Cosmos de la Universitat de Barcelona, ICCUB, 08028 Barcelona, Spain

★ [simone.cantori@unicam.it](mailto:simone.cantori@unicam.it),

## Abstract

Estimating ground-state energies of quantum many-body systems is challenging due to the exponential growth of Hilbert space. Sample-based diagonalization (SBD) addresses this by projecting the Hamiltonian onto a subspace of selected basis configurations but works only for concentrated ground-state wave functions. We propose two neural network-enhanced SBD methods: sample-based neural diagonalization (SND) and adaptive-basis SND (AB-SND). Both leverage autoregressive neural networks for efficient sampling; AB-SND also optimizes a basis transformation to concentrate the wave function. We explore classically tractable single- and two-spin rotations, and more expressive unitaries implementable on quantum computers. On quantum Ising models, SND performs well for concentrated states, while AB-SND consistently outperforms SND and standard SBD in less concentrated regimes.

Copyright attribution to authors.

This work is a submission to SciPost Physics.

License information to appear upon publication.

Publication information to appear upon publication.

Received Date

Accepted Date

Published Date

1

## Contents

1	Introduction	2
2	Methods	4
3	Results	5
4	Basis change using a quantum computer	9
5	Conclusions	9
A	Loss function of SND and its gradient	11
B	Loss function of AB-SND and its gradient	11

10	<b>C Failure of standard SBD approaches at large transverse field</b>	<b>12</b>
11	<b>D Most challenging regime for AB-SND</b>	<b>13</b>
12	<b>E Loss function of AB-SND with sampled rotational parameters</b>	<b>13</b>
13	<b>F Problem of sampling unique configurations</b>	<b>14</b>
14	<b>G Autoregressive neural network and hyperparameters</b>	<b>15</b>
15	<b>References</b>	<b>17</b>

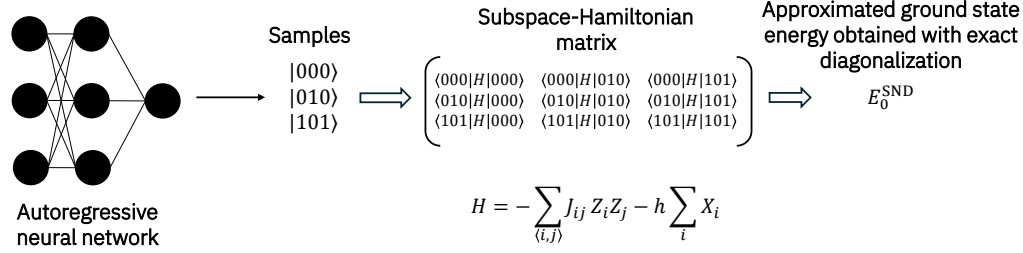
## 18 1 Introduction

19 The accurate calculation of ground-state properties of quantum many-body systems is one of  
 20 the central challenges in quantum chemistry and condensed matter physics. The exponen-  
 21 tial growth of the Hilbert space with the system size makes exact solutions intractable for  
 22 large systems, necessitating the development of approximate computational methods. Deep  
 23 learning methods have emerged as promising tools to address this challenge [1–3]. For ex-  
 24 ample, supervised learning approaches have been used to predict ground-state energies based  
 25 on labeled training data [4–7]. On the other hand, the introduction of neural quantum states  
 26 (NQS), which represent wave functions using neural network (NN) architectures, has opened  
 27 new possibilities for variational Monte Carlo simulations, circumventing the need of labeled  
 28 data [8–10].

29 In quantum chemistry, a standard approach to tackle the problem of the Hilbert space size  
 30 is represented by selected configuration interaction methods [11–14]. These employ prede-  
 31 fined wave-function ansatzes, Monte Carlo sampling, or other empirical criteria to select a set  
 32 of relevant basis configurations  $|x^{(l)}\rangle$ , labeled by the index  $l$ . The corresponding Hamiltonian  
 33 matrix elements  $\langle x^{(l)}|H|x^{(m)}\rangle$  are evaluated to define a subspace Hamiltonian matrix. The  
 34 ground-state energy is then approximated by computing the lowest eigenvalue of this matrix.  
 35 Recently, these approaches have also been adopted in the context of quantum computing, un-  
 36 der the name of Sample-based Diagonalization (SBD) [15–17]. The key idea is to employ  
 37 quantum circuits to sample relevant configurations, leading to what is dubbed Sample-based  
 38 Quantum Diagonalization (SQD). In principle, quantum circuits might allow for the sampling  
 39 of classically intractable distributions [18]. Machine learning algorithms have also been used  
 40 to select relevant configurations [19–22]. Yet, the problem of how to efficiently truncate the  
 41 Hilbert space, while minimizing the introduced approximation, is still open. In fact, SBD ap-  
 42 proaches are known to perform well only when the ground-state wave function is concentrated  
 43 on the chosen computational basis [15], which means that its amplitudes are not negligible  
 44 only on a small subset of basis elements. This strongly limits the regime of applicability of SBD  
 45 methods.

46 In this article, we introduce two NN enhanced SBD approaches: sample-based neural  
 47 diagonalization (SND) and its extension based on an adaptive basis, which we refer to as  
 48 adaptive-basis SND (AB-SND). Both methods employ autoregressive NNs to efficiently sample  
 49 basis configurations relevant for the estimation of the ground-state energy, as illustrated in  
 50 Fig. 1. While SND operates in a fixed computational basis, AB-SND incorporates a basis trans-  
 51 formation, allowing for improved performance when the ground state is not concentrated in

## Sample-based neural diagonalization (SND):



## Adaptive-basis - sample-based neural diagonalization (AB-SND):

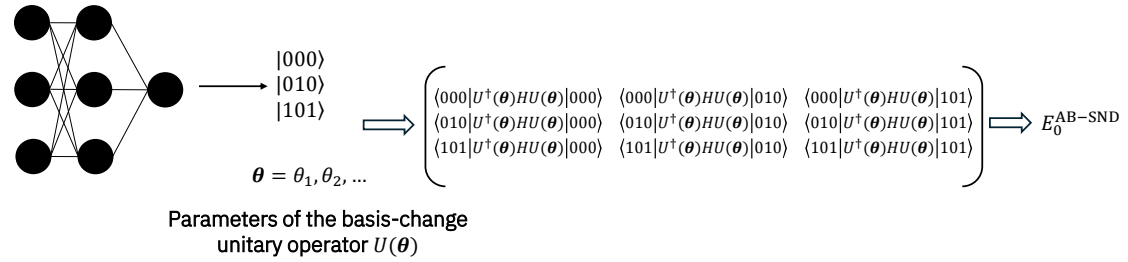


Figure 1: Scheme of the SND and AB-SND methods. In SND (top), an autoregressive neural network generates the bitstrings that define the subspace for diagonalization. In AB-SND (bottom), we also optimize some basis-transformation parameters  $\theta$ , enabling us to perform sampling in a rotated basis where the ground state is more concentrated.

the original computational basis, a regime in which standard SBD techniques are doomed to fail. In our implementation, the basis change is performed using parameterized single-spin and two-spin rotations, which are efficiently computable on classical hardware. Additionally, we explore more expressive basis transformations, describing how quantum computers allow their implementation for large systems. The testbeds we consider are one-dimensional (1D) and two-dimensional (2D) ferromagnetic quantum Ising models and a 2D quantum spin-glass model. These models are chosen because the concentration of their ground state can be tuned, allowing us to test SBD approaches in different regimes of computational hardness, and because the benchmark ground-state energy can be exactly computed. Notably, we find that the AB-SND approach allows us to considerably extend the regime of applicability of SBD methods, in particular, when performed with the more general basis transformations.

The rest of this article is organized as follows: Sec. 2 provides the details of the methodology of both SND and AB-SND. Sec. 3 presents our numerical results for different quantum Ising models, comparing the performance of the proposed approaches to standard SBD techniques based on sampling from NQS variational ansatzes. In Sec. 4, we discuss the possibility of implementing AB-SND using quantum hardware, highlighting its potential for hybrid quantum-classical schemes. In Sec. 5, we summarize our findings and discuss future directions. Finally, the Appendices provide additional details on: the definition of the loss functions and their gradient calculations for SND (Appendix A) and AB-SND (App. B); the failure of standard SBD when the ground state is not concentrated (App. C); the regime of maximum error in AB-SND (App. D); the optimization of angle parameters via stochastic sampling (App. E); the effective temperature scaling for efficient sampling of unique configurations (App. F); the autoregressive NN architectures (App. G).

## 2 Methods

As in standard SBD approaches, the SND methods we introduce hereafter aim to approximate the ground-state energy of a quantum system by projecting the Hamiltonian onto a subspace spanned by a selected set of basis configurations. In our implementation, these configurations are selected from the standard computational basis, which consists of tensor products of the single-qubit basis states  $|0\rangle$  and  $|1\rangle$ , namely, the eigenstates of the Pauli-Z operator. For a system of  $N$  spins, the computational basis states  $|x\rangle = |x_1 x_2 \dots x_N\rangle$  correspond to bitstrings  $x$ , where each component  $x_i \in \{0, 1\}$ . Given a set of  $S$  unique configurations,  $\{|x^{(l)}\rangle\}_{l=1,\dots,S}$ , one constructs a subspace Hamiltonian by evaluating the matrix elements  $\langle x^{(l)} | H | x^{(m)} \rangle$ . The lowest eigenvalue  $E$  of this subspace matrix provides a variational upper bound for the ground-state energy, which converges to the exact value for  $S \rightarrow 2^N$ . Clearly, this limit is computationally impractical for system sizes  $N \gg 10$ . Yet, suitable criteria to select the subset of basis configurations lead to accurate approximations for feasible value of  $S$ .

In our framework, the selected configurations are sampled using autoregressive NNs, which can be trained to minimize  $E$ . More precisely, as in Ref. [15], we define the loss function to be minimized during training as

$$L = \sum_k P(S^{(k)}) E^{(k)}, \quad (1)$$

where  $S^{(k)}$  represents a batch of bitstrings and  $E^{(k)}$  is the lowest eigenvalue of the subspace Hamiltonian built on the  $k$ -th batch of bitstrings. In our case, the probability  $P(S^{(k)})$  of sampling  $S^{(k)}$  is given by the autoregressive NN. The minimization is performed using stochastic gradient-based methods, and the derivation of the gradient of  $L$  with respect to the weights of the NN is shown in the Appendix A.

The testbeds considered in this article are quantum Ising models described by the following Hamiltonian:

$$H = - \sum_{\langle i,j \rangle} J_{ij} Z_i Z_j - h \sum_i X_i, \quad (2)$$

where  $Z_i$  and  $X_i$  are Pauli operators acting on spin  $i$ ,  $J_{ij}$  represents the interaction strength between the nearest-neighbor spins  $i$  and  $j$ , and  $h$  is the transverse field strength. Specifically, we consider three variants of this model:

1. 1D ferromagnetic transverse field Ising model (1D-TFIM), with  $J_{ii+1} = 1$  for  $i = 1, \dots, N$ , and periodic boundary conditions, i.e., the spin  $N + 1$  is identified with the spin 1;
2. 2D ferromagnetic TFIM (2D-TFIM), with  $J_{ij} = 1$  for  $i$  and  $j$  nearest-neighbor spins on a square lattice, and open boundary conditions;
3. 2D Edward-Anderson model (2D-EAM) on a square lattice, with  $J_{ij}$  randomly sampled from a normal distribution  $\mathcal{N}(0, 1)$  with zero mean and unit variance, and periodic boundary conditions.

It is worth pointing out that quantum Monte Carlo simulations of quantum Ising models are not affected by the negative sign problem. Thus, by adopting these models as testbeds for the SBD approaches, we have the opportunity to make comparisons against unbiased estimates of the ground-state energy, even beyond the 1D case where the Jordan-Wigner theory provides the exact solution. In particular, the 2D-EAM represents a challenging testbed due to the presence of disordered frustrated interactions. In addition, tuning  $h$  allows us to control the concentration of the ground state [23], thus testing the SBD approaches in different regimes. Indeed, for  $h \rightarrow \infty$ , the ground state of these models tends to an equally weighted superposition of the computational basis elements, i.e.  $|++\dots+\rangle$  (with  $|+\rangle = \frac{1}{\sqrt{2}}(|0\rangle + |1\rangle)$ ). In the opposite limit  $h \rightarrow 0$ , quantum fluctuations vanish, leading to a more concentrated ground-state

118 wave function in the chosen computational basis. It is worth emphasizing that generic SBD  
 119 methods, including our SND method without adaptive basis changes, are expected to perform  
 120 well only for relatively small  $h$ . Numerical results confirming this expectation are shown in  
 121 the Appendix A.

122 To extend the regime of applicability of SBD approaches, we introduce the AB-SND method.  
 123 AB-SND improves the SND strategy by incorporating a basis transformation defined by a pa-  
 124 rameterized unitary operator  $U(\boldsymbol{\theta})$ , which maps the original computational basis to a rotated  
 125 basis in which the ground state is more concentrated. As in SND, an autoregressive NN gen-  
 126 erates bitstring samples, but these are rotated by  $U(\boldsymbol{\theta})$ . The subspace Hamiltonian is then  
 127 constructed from transformed matrix elements  $\langle x^{(l)} | U(\boldsymbol{\theta})^\dagger H U(\boldsymbol{\theta}) | x^{(m)} \rangle$ , as shown in Fig. 1. In  
 128 most of our experiments, we use a combination of single-spin rotations  $U(\boldsymbol{\theta}) = \bigotimes_{i=1,\dots,N} U_i(\theta_i)$ ,  
 129 where

$$U_i(\theta_i) = \begin{bmatrix} \cos \frac{\theta_i}{2} & -\sin \frac{\theta_i}{2} \\ \sin \frac{\theta_i}{2} & \cos \frac{\theta_i}{2} \end{bmatrix}, \quad (3)$$

130 and each angle  $\theta_i$  is an independent parameter for spin  $i$ . Because the rotations act indepen-  
 131 dently on each spin and the Hamiltonian is composed of local Pauli operators, we can effi-  
 132 ciently compute the transformed Hamiltonian  $U^\dagger H U$  using classical hardware. In addition to  
 133 single-spin rotations, we also implement non-overlapping two-spin rotations, which increase  
 134 the expressive power of the basis transformation while remaining classically tractable. The  
 135 unitary operator is defined as a composition of  $R_Y$ ,  $R_{ZZ}$ , and  $R_X$  gates that act on each spin in  
 136 the pair. The matrix representations of these gates are as follows:

$$R_Y(\alpha) = \begin{bmatrix} \cos \frac{\alpha}{2} & -\sin \frac{\alpha}{2} \\ \sin \frac{\alpha}{2} & \cos \frac{\alpha}{2} \end{bmatrix},$$

$$R_X(\beta) = \begin{bmatrix} \cos \frac{\beta}{2} & -i \sin \frac{\beta}{2} \\ -i \sin \frac{\beta}{2} & \cos \frac{\beta}{2} \end{bmatrix}, \quad (4)$$

$$R_{ZZ}(\gamma) = \begin{bmatrix} e^{-i\frac{\gamma}{2}} & 0 & 0 & 0 \\ 0 & e^{i\frac{\gamma}{2}} & 0 & 0 \\ 0 & 0 & e^{i\frac{\gamma}{2}} & 0 \\ 0 & 0 & 0 & e^{-i\frac{\gamma}{2}} \end{bmatrix}.$$

137 As mentioned above, the gates  $R_{ZZ}(\gamma)$  act on non-overlapping spin pairs  $\{0, 1\}$ ,  $\{2, 3\}$ , etc.  
 138 However, the AB-SND framework is compatible with more general, potentially strongly entan-  
 139 gling basis transformations, which could be implemented on quantum hardware. The use of  
 140 quantum circuits for evaluating subspace matrix elements is discussed in Sec. 4. For AB-SND,  
 141 the optimization of the angle parameter  $\boldsymbol{\theta}$  can be approached in different ways, as discussed  
 142 in the Appendices B and E.

### 143 3 Results

144 Hereafter, we analyze the performances of SND and AB-SND powered by local basis transfor-  
 145 mations on the three quantum spin models described in Sec. 2. As a benchmark, we consider  
 146 a more standard SBD approach in which the configurations are sampled from the (squared  
 147 modulus) exact ground-state wave function or from a very accurate approximation obtained  
 148 via a variational Monte Carlo simulation. It is worth emphasizing that this procedure assumes

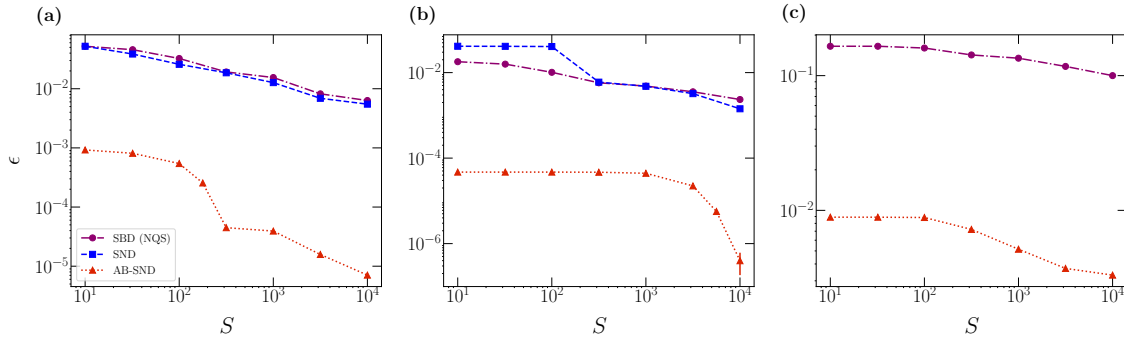


Figure 2: Relative error  $\epsilon$  as a function of the number of unique configurations  $S$  used to build the subspace Hamiltonian. Panels (a), (b), and (c) display the relative errors for the 1D-TFIM, the 2D-TFIM, and the 2D-EAM with  $N = 50$ ,  $N = 100$ , and  $N = 64$  spins, respectively. The transverse field is  $h = 0.5$  for the 1D-TFIM and the 2D-TFIM, while it is  $h = 1$  for the 2D-EAM. In panel (b), we take into account the statistical uncertainty of the quantum Monte Carlo simulations used to determine the unbiased estimate of the ground-state energy.

that an accurate representation of the ground state can be obtained through a complementary computational technique. This allows us to execute standard SBD under very favorable conditions, thus representing a stringent benchmark for novel SND approaches. We sample configurations from an NQS in the form of a restricted Boltzmann machine. The latter is optimized using the NetKet library [24, 25]. Our numerical tests show that, as a sampling engine for SBD approaches, the NQS ansatz performs essentially as well as the exact ground state, at least for the system sizes for which the latter can be computed. Thus, in the following, we mostly adopt NQS sampling, unless otherwise specified.

To quantify the performance of the various SBD approaches, we compute the relative error  $\epsilon = |\frac{y - E_0}{E_0}|$ , where  $y$  represents the energy estimate from a given method, and  $E_0$  is the exact ground-state energy. The latter is computed via the Jordan-Wigner transformations for the 1D model [26, 27], while for the 2D models we employ continuous-time projection quantum Monte Carlo simulations [28, 29]. The latter provide unbiased estimates, affected only by very small statistical uncertainties.

In Fig. 2, we analyze the relative errors in the three testbed models, considering relatively weak transverse fields  $h$  for which the ground state is concentrated in the chosen computational basis. As expected, all three SBD techniques perform well, showing a systematic accuracy improvement with the number of unique configurations  $S$  used to build the subspace. However, the SND performance deteriorates for the 2D-EAM (not shown). This effect may be attributed to the rugged energy landscapes occurring in spin-glass phases [30]. In this testbed, the standard SBD method based on NQS-sampled configurations performs better, but still reaches errors as large as 10% for computationally practical values of  $S$ . Notably, thanks to the additional variational flexibility introduced by the learnable basis transformation, the AB-SND method displays a systematic performance improvement with  $S$  also in the 2D-EAM. In fact, it consistently outperforms the other SBD approaches we consider, in all three testbeds.

In Fig. 3, the relative energy error is plotted as a function of the transverse field  $h$ , for different numbers of unique configurations  $S$ . As expected, the performance of SND and standard NQS-based SBD methods rapidly deteriorates as  $h$  increases, denoting the limited regime of applicability of these approaches. Instead, the AB-SND method, here implemented with single-spin rotations, is accurate also at significantly larger transverse fields. In fact, it reaches small relative errors also in the large  $h$  limit. This indicates that adaptive single-spin rotations enable a continuous interpolation between the original computational basis, in which



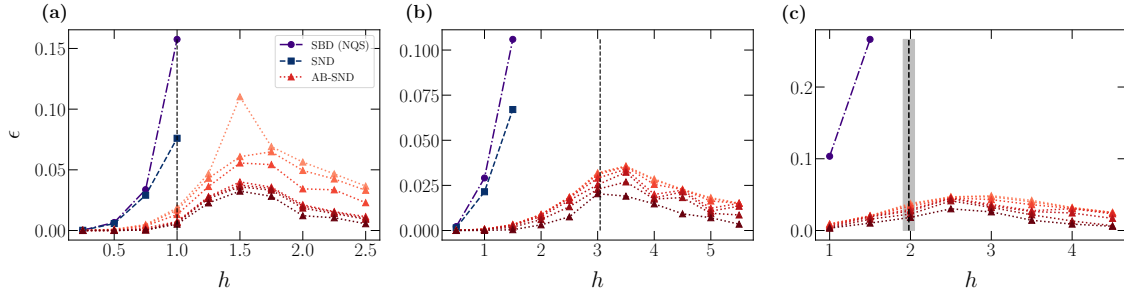


Figure 3: Relative error  $\epsilon$  as a function of the transverse field  $h$ , for different numbers of unique configurations  $S$ . For AB-SND, darker colors correspond to larger  $S$ , with  $S \in \{10, 10^{1.5}, 10^2, \dots, 10^4\}$ , while for SBD from the NQS and SND we consider only  $S = 10^4$ . Panel (a) represents the errors for the 1D-TFIM with  $N = 50$  spins, panel (b) corresponds to the 2D-TFIM with  $N = 100$  spins, and panel (c) to the 2D-EAM with  $N = 64$  spins. The vertical dashed lines represent the corresponding quantum critical points, namely, the ferromagnetic transitions in the 1D-TFIM and the 2D-TFIM, and the spin-glass transition in the 2D-EAM. For the latter, the uncertainty is represented by the gray bar [29].

the ground state is concentrated in the  $h \rightarrow 0$  limit, and the basis built using eigenstates of the  $X$  Pauli operator  $|+\rangle, |-\rangle$ , in which concentration occurs in the opposite limit. Sizable inaccuracies occur in the intermediate regime, approximately in the region around the quantum phase transitions occurring in the three testbed models, namely, the paramagnetic to ferromagnetic transition in the 1D-TFIM and the 2D-TFIM, and the quantum spin-glass transition in the 2D-EAM [29]. In the Appendix D, we provide numerical evidence that in the large  $S$  limit, the peak of the energy error approaches the critical point  $h_c = 1$  of the 1D-TFIM.

In Fig. 4, we analyze how the computational cost scales with the system size  $N$ . Specifically, we determine the number of unique configurations  $S$  required to reach a relative error of 1%, considering the 1D-TFIM. A standard SBD approach based on NQS sampling displays a problematic scaling already for  $h \gtrsim 0.5$ , making it impractical to reach system sizes  $N \simeq 100$  keeping the target accuracy. In this regime, the number of configurations required by the AB-SND approach powered by single-spin rotations is still essentially independent of  $N$ , denoting the important role of the basis change. However, the scaling approaches an exponential behavior slightly beyond the critical point  $h_c = 1$ , while it improves again for transverse fields  $h \gg 1$ . Better accuracies in the critical regime  $h \simeq 1$  can be obtained within the AB-SND approach with more general basis transformations, as discussed in the following.

In Fig. 5, we compare the accuracies of the AB-SND approaches powered by single-spin rotations and by non-overlapping two-spin unitary operators. The latter approach allows introducing some entanglement and provides a more expressive basis transformation, while remaining classically tractable. In fact, we find that, at and slightly beyond the critical regime  $h \gtrsim 1$ , two-spin rotations lead to a sizable accuracy improvement compared to the single-spin case and, of course, compared to standard SBD based on the NQS-approximated ground-state sampling. Even better accuracies can be obtained by implementing classically intractable basis transformations using quantum hardware, as discussed in Section 4.

An additional important challenge for all stochastic SBD methods is the decreasing efficiency of sampling unique configurations as the number of samples increases. This phenomenon, also noted in Ref. [31], can be addressed in our framework through effective temperature scaling during inference. This procedure is discussed in Appendix F).

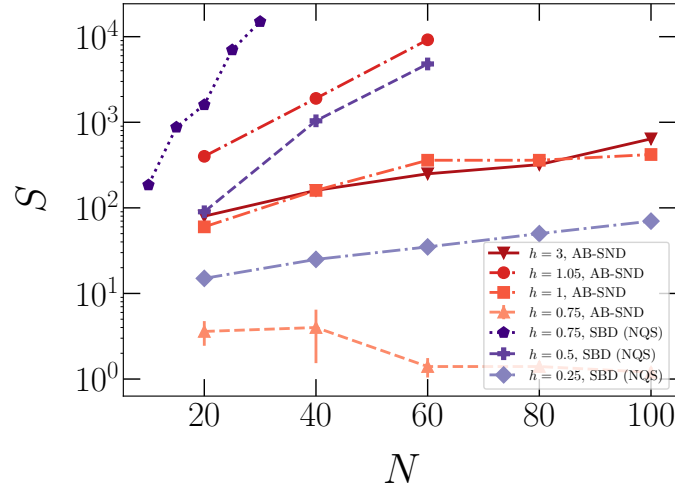


Figure 4: Number of unique configurations  $S$  required to reach relative errors below  $\epsilon = 0.01$  as a function of the number of spins  $N$  for the 1D-TFIM at different transverse fields  $h$ . We compare the performance of a standard SBD approach powered by NQS sampling (shades of blue) with the one of the AB-SND with single-spin rotations (shades of red). The error-bars for the AB-SND method for  $h = 0.5$  and  $h = 0.75$  represent the estimated standard deviation of the average over five training processes.

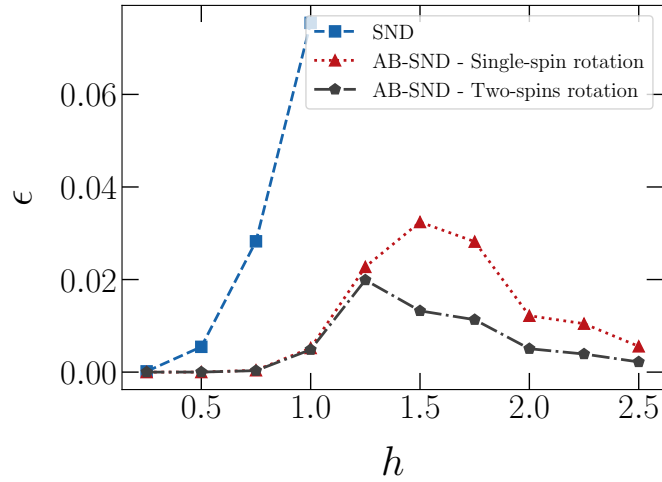


Figure 5: Relative error  $\epsilon$  as a function of transverse field  $h$ , for  $S = 10^4$  unique configurations in the truncated basis. The testbed is the 1D-TFIM with  $N = 50$  spins. We compare the performances of the SND approach, with the ones of AB-SND approaches featuring single-spin and non-overlapping two-spin rotations.



## 210 4 Basis change using a quantum computer

211 For the quantum Ising models we consider, which feature up to two-spin couplings, basis  
 212 changes based on combinations of single-spin and non-overlapping two-spin transformations  
 213 can be efficiently performed on classical computers. More expressive basis changes could be  
 214 efficiently performed using quantum circuits. Such transformations could further improve the  
 215 performance of AB-SND approaches, especially near critical points. Indeed, a variational quan-  
 216 tum eigensolver (VQE) algorithm has been shown to be able to accurately solve the 1D-TFIM  
 217 also at criticality by optimizing a unitary transformation  $U(\boldsymbol{\theta})$ . This is achieved by minimiz-  
 218 ing the expectation value  $\langle 0|U^\dagger(\boldsymbol{\theta})HU(\boldsymbol{\theta})|0\rangle$  [32], which is estimated using (typically large)  
 219 shot numbers. This is equivalent to a specific AB-SND strategy with only a single sampled  
 220 configuration, namely, the state  $|0\rangle = |00\dots 0\rangle$ . The general AB-SND approach extends VQE  
 221 by including the sampling of more basis elements, which leads to a finite matrix whose lowest  
 222 eigenvalue is to be determined. Hereafter, we discuss how to implement a generic basis-  
 223 change procedure using quantum computers. First, we set up a quantum circuit representing  
 224 a parametrized basis-change unitary operator  $U(\boldsymbol{\theta})$ . Then, we can calculate the subspace-  
 225 Hamiltonian elements  $\langle x^{(l)}|U^\dagger(\boldsymbol{\theta})HU(\boldsymbol{\theta})|x^{(m)}\rangle$  using the approach introduced in Ref. [33].  
 226 The diagonal terms  $H_l = \langle x^{(l)}|U^\dagger(\boldsymbol{\theta})HU(\boldsymbol{\theta})|x^{(l)}\rangle$  can be computed as standard expectation  
 227 values. The off-diagonal terms can be calculated noticing that (using  $i = \sqrt{-1}$ )

$$\Re\langle x^{(l)}|U^\dagger(\boldsymbol{\theta})HU(\boldsymbol{\theta})|x^{(m)}\rangle = H_{l+m} - \frac{H_l}{2} - \frac{H_m}{2}, \quad (5)$$

228 and

$$\Im\langle x^{(l)}|U^\dagger(\boldsymbol{\theta})HU(\boldsymbol{\theta})|x^{(m)}\rangle = -H_{l+im} + \frac{H_l}{2} + \frac{H_m}{2}, \quad (6)$$

229 where

$$H_{l+m} = \frac{1}{\sqrt{2}}(\langle x^{(l)}| + \langle x^{(m)}|)U^\dagger(\boldsymbol{\theta})HU(\boldsymbol{\theta})\frac{1}{\sqrt{2}}(|x^{(l)}\rangle + |x^{(m)}\rangle) \quad (7)$$

230 and

$$H_{l+im} = \frac{1}{\sqrt{2}}(\langle x^{(l)}| - i\langle x^{(m)}|)U^\dagger(\boldsymbol{\theta})HU(\boldsymbol{\theta})\frac{1}{\sqrt{2}}(|x^{(l)}\rangle + i|x^{(m)}\rangle). \quad (8)$$

231 Finally, in our framework, both the parameters  $\boldsymbol{\theta}$  and the weights of the autoregressive NN  
 232 from which the bitstrings  $x^{(l)}$  are sampled can be optimized as explained for the AB-SND  
 233 procedure with single-spin rotations. To test this approach, we implement a small numerical  
 234 experiment using a classical simulation of quantum circuits with  $N = 6$  qubits for the 1D-TFIM.  
 235 The circuit ansatz we choose is rather shallow. It features one layer of  $R_Y$  gates acting on each  
 236 qubit, and two blocks including  $R_{ZZ}$  operators acting on all nearest-neighbor pairs and  $R_X$   
 237 rotations acting on each qubit. As shown in Fig. 6, the improvement of the AB-SND predictions  
 238 based on the circuit-based basis change compared with the case of single-spin transformations  
 239 is significant. With the more general transformation, appreciable inaccuracies occur only very  
 240 close to the critical point  $h_c = 1$ . We expect even better performances to be obtained by  
 241 implementing basis transformations using deeper quantum circuits.

## 242 5 Conclusions

243 In this article, we introduced SND and its basis-adaptive extension, dubbed AB-SND. These are  
 244 two NN-assisted sample-based diagonalization techniques for estimating ground-state energies  
 245 of quantum many-body systems. Our tests show that AB-SND offers significant improvements  
 246 over conventional SBD methods, particularly in regimes where the ground state is delocalized  
 247 in the computational basis.

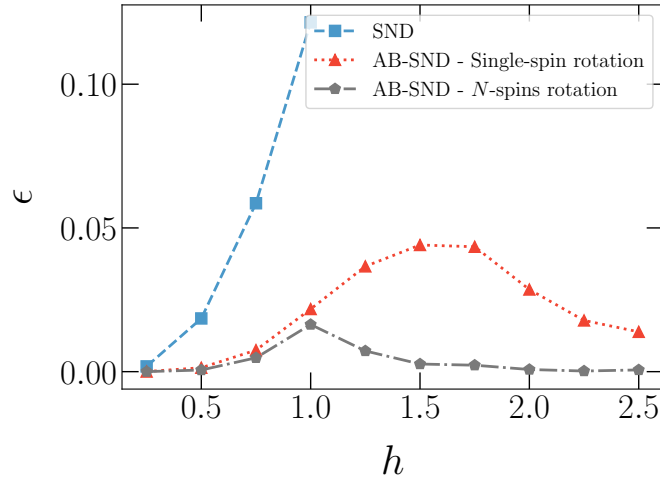


Figure 6: Relative error  $\epsilon$  as a function of the transverse field  $h$ , for  $S = 16$  unique configurations. The testbed model is the 1D-TFIM with  $N = 6$  spins. We compare the accuracies of the SND approach with the ones of the AB-SND methods with single-spin rotations and with a general basis change performed by the (simulated) quantum circuit described in the text.

248 To extend the AB-SND approach beyond basis changes based on single-spin and two-spin  
 249 operators, we explored the integration of AB-SND with quantum computing. As we explained,  
 250 this allows the implementation of more general basis transformations. To test this procedure,  
 251 we implemented a small-scale proof-of-concept experiment using classically simulated quan-  
 252 tum circuits. In this setting, we used parametrized entangling gates to define a more expressive  
 253 unitary  $U(\theta)$ , which led to improved performance compared to local spin rotations. Although  
 254 these results are currently limited to small systems simulated classically, they suggest that AB-  
 255 SND can be extended to hybrid quantum-classical workflows and could benefit from access  
 256 to real quantum hardware in the future. In fact, the AB-SND approach driven by quantum  
 257 circuits represents an extension of the VQE algorithm beyond the case of a single initial state.

258 Further developments could include the use of more expressive basis-change circuits, im-  
 259 proved optimization strategies in complex energy landscapes, and systematic explorations of  
 260 the performance of AB-SND methods in larger or more strongly correlated systems. By com-  
 261 bining neural sampling with learnable basis transformations, AB-SND provides a flexible and  
 262 scalable framework for studying quantum many-body problems across a wide range of regimes.

263 The essential scripts used in this study are available on GitHub [34].

## 264 Acknowledgements

265 **Funding information** Support from the following sources is acknowledged: PNRR MUR  
 266 project PE0000023-NQSTI; PRIN 2022 MUR project “Hybrid algorithms for quantum simula-  
 267 tors” – 2022H77XB7; PRIN-PNRR 2022 MUR project “UEFA” – P2022NMBAJ; National Cen-  
 268 tre for HPC, Big Data and Quantum Computing (ICSC), CN00000013 Spoke 7 – Materials &  
 269 Molecular Sciences, under project INNOVATOR; CINECA awards ISCRA IsCc2\_REASON and  
 270 INF25\_lincoln, for the availability of high-performance computing resources and support; Eu-  
 271 roHPC Joint Undertaking for awarding access to the EuroHPC supercomputer LUMI, hosted  
 272 by CSC (Finland), through EuroHPC Development and Regular Access calls. E.R. acknowl-  
 273 edges support from the Catalonia Quantum Academy Student Research Fellowship 2024 for

his research internship at the University of Barcelona.

## A Loss function of SND and its gradient

As in Eq. (1), one can write the probability of a set of configurations  $S^{(k)}$  as  $P(S^{(k)}) = \prod_{x^{(l)} \in S^{(k)}} P(x^{(l)})$ , where  $P(x^{(l)})$  is the probability of sampling the bitstring  $x^{(l)}$  defined by an autoregressive NN. The loss function  $L$  and its derivative with respect to a parameter of the network  $\omega$  can be calculated as follows:

$$\begin{aligned} L &= \sum_k \left( \prod_{x^{(l)} \in S^{(k)}} P(x^{(l)}) \right) E^{(k)} \Rightarrow \\ \frac{\partial L}{\partial \omega} &= \sum_k \frac{\partial}{\partial \omega} \left( \prod_{x^{(l)} \in S^{(k)}} P(x^{(l)}) \right) E^{(k)} \\ &= \sum_k \left[ \sum_{x^{(l)} \in S^{(k)}} \left( \frac{\partial P(x^{(l)})}{\partial \omega} \prod_{x^{(m)} \neq x^{(l)}} P(x^{(m)}) \right) \right] E^{(k)}, \end{aligned} \quad (\text{A.1})$$

where  $x^{(l)}$  and  $x^{(m)}$  are bitstrings in the batch  $S^{(k)}$ . With a straightforward rearrangement, the derivative can be rewritten as

$$\begin{aligned} \frac{\partial L}{\partial \omega} &= \sum_k \left[ \sum_{x^{(l)} \in S^{(k)}} \left( \frac{\partial P(x^{(l)})}{\partial \omega} \frac{P(x^{(l)})}{P(x^{(l)})} \prod_{x^{(m)} \neq x^{(l)}} P(x^{(m)}) \right) \right] E^{(k)} \\ &= \sum_k P(S^{(k)}) \left( \sum_{x^{(l)} \in S^{(k)}} \frac{\partial \log(P(x^{(l)}))}{\partial \omega} \right) E^{(k)}, \end{aligned} \quad (\text{A.2})$$

and the stochastic estimator is given by

$$\frac{\partial L}{\partial \omega} \simeq \frac{1}{K} \sum_{k=1}^K \left( \sum_{x^{(l)} \in S^{(k)}} \frac{\partial \log(P(x^{(l)}))}{\partial \omega} \right) E^{(k)}, \quad (\text{A.3})$$

where the batches of bitstrings  $S^{(k)}$  are sampled according to  $P(S^{(k)})$ . A baseline term is useful to stabilize the training process [9, 10]. In our framework, we set it equal to the average energy over the  $K$  batches  $\overline{E^{(k)}}$ . Therefore, the loss function for SND reads:

$$L = \frac{1}{K} \sum_{k=1}^K \left( \sum_{x^{(l)} \in S^{(k)}} \log(P(x^{(l)})) \right) (E^{(k)} - \overline{E^{(k)}}). \quad (\text{A.4})$$

## B Loss function of AB-SND and its gradient

For the AB-SND method, the derivative with respect to the parameters of the NN used to sample basis configurations  $\frac{\partial L}{\partial \omega}$  is calculated as discussed in the previous section. However, here we also want to optimize the basis-change parameters  $\theta$  in order to minimize the estimated ground-state energy. Notably, the rotation angles  $\theta$  are also used as a condition for the NN that generates the spin configurations. For this, they are provided as inputs preceding the spin values. Similarly to the SND method, one obtains:

$$\frac{\partial L}{\partial \theta_i} = \sum_k \frac{\partial}{\partial \theta_i} \left( \prod_{x^{(l)} \in S^{(k)}} P(x^{(l)} | \theta) \right) E^{(k)} + \left( \prod_{x^{(l)} \in S^{(k)}} P(x^{(l)} | \theta) \right) \frac{\partial}{\partial \theta_i} E^{(k)}. \quad (\text{B.1})$$

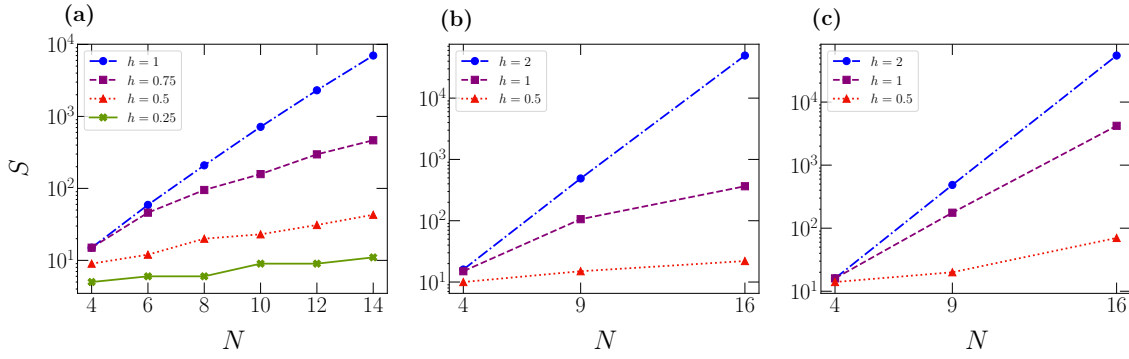


Figure 7: Number of unique configurations  $S$  required to reach the relative error  $\epsilon = 0.01$  as a function of number of spins  $N$  using a standard SBD approach with configurations sampled from the exact ground state. Panels (a), (b), and (c) display results for the 1D-TFIM, the 2D-TFIM, and the 2D-EAM, respectively. Different datasets in each panel correspond to different transverse fields  $h$ .

293 From the Hellmann–Feynman theorem, one can write

$$\frac{\partial E^{(k)}(\theta_i)}{\partial \theta_i} = \left\langle \psi_0^{(k)} \left| \frac{\partial \hat{H}}{\partial \theta_i} \right| \psi_0^{(k)} \right\rangle, \quad (\text{B.2})$$

294 where  $\psi_0^{(k)}$  is the estimated ground-state wave function. In AB-SND, we use a basis-change  
295 unitary operator  $U(\boldsymbol{\theta})$ , so

$$\frac{\partial E^{(k)}(\theta_i)}{\partial \theta_i} = \left\langle \psi_0^{(k)} \left| \frac{\partial (U^\dagger(\boldsymbol{\theta}) \hat{H} U(\boldsymbol{\theta}))}{\partial \theta_i} \right| \psi_0^{(k)} \right\rangle. \quad (\text{B.3})$$

296 This quantity can be calculated using the parameter-shift rule [35, 36]. Alternatively, if  $U(\boldsymbol{\theta})$   
297 is implemented using classical algorithms, the gradient can be calculated using automatic  
298 differentiation, e.g., via the Pytorch library [37]. Finally, the derivative with respect to a  
299 generic rotation angle reads:

$$\frac{\partial L}{\partial \theta_i} \simeq \frac{1}{K} \sum_{k=1}^K \left[ \left( \sum_{x^{(l)} \in S^{(k)}} \frac{\partial \log(P(x^{(l)} | \boldsymbol{\theta}))}{\partial \theta_i} \right) E^{(k)} + \left\langle \psi_0^{(k)} \left| \frac{\partial (U^\dagger(\boldsymbol{\theta}) \hat{H} U(\boldsymbol{\theta}))}{\partial \theta_i} \right| \psi_0^{(k)} \right\rangle \right]. \quad (\text{B.4})$$

300 We also implement an alternative approach to optimize the rotation angles, which avoids the  
301 multiple diagonalization steps used in the parameter-shift rule. This approach involves sam-  
302 pling the angles  $\boldsymbol{\theta}$  from an additional autoregressive NN. It is detailed in Appendix E.

## 303 C Failure of standard SBD approaches at large transverse field

304 The accuracy of SBD approaches noticeably depends on how the computational basis elements  
305 used to build the truncated Hamiltonian matrix are sampled. In Fig. 7, we show that even when  
306 the exact ground-state wave function is used for sampling, without adaptive basis rotations  
307 the SBD method fails when the ground-state wave function is not strongly concentrated in  
308 the chosen computational basis. In fact, beyond the small transverse field regime  $h \ll 1$ , the  
309 truncated basis size  $S$  required to reach the target accuracy of 1% approaches an exponential  
310 scaling with the system size  $N$ .

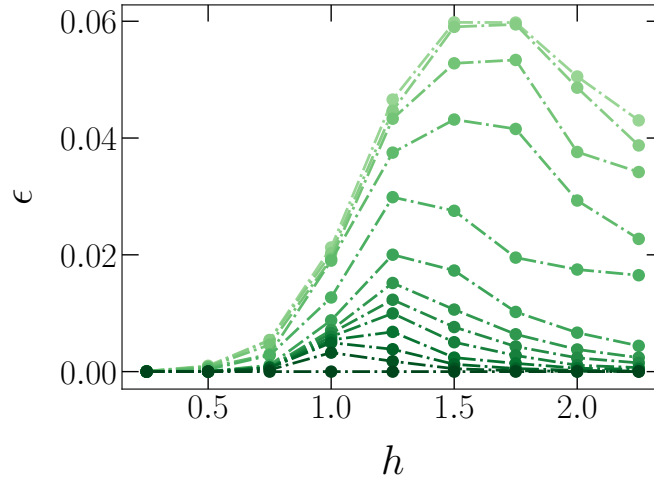


Figure 8: Relative error  $\epsilon$  as a function of the transverse field  $h$ , for different numbers of unique configuration  $S$ . Darker colors mean higher  $S$ , with  $S \in \{4, 8, 16, 32, 64, 128, 256, 384, 512, 640, 768, 896, 1024\}$ . The configurations are sampled from the exact ground state. Adaptive single-spin rotations are then applied, as explained in the main text. These results are for the 1D-TFIM with  $N = 10$  spins.

## 311 D Most challenging regime for AB-SND

312 In Fig. 8 we report numerical evidence showing that, in the large  $S$  limit, the peak of the  
 313 energy error obtained via the AB-SND method drifts towards the critical point of the ferro-  
 314 magnetic quantum phase transition. The chosen testbed is the 1D-TFIM with  $N = 10$  spins.  
 315 The configurations are sampled from the exact ground state.

## 316 E Loss function of AB-SND with sampled rotational parameters

317 Instead of optimizing the basis change using the Hellmann–Feynman theorem, one can em-  
 318 ploy an additional autoregressive NN to sample the parameters  $\theta$  that define the basis-change  
 319 unitary operator. In this alternative procedure, the probability of a set of spin configurations  
 320 is written as:  $P(S^{(k)}) = P_{\nu}(\theta^{(k)})P_{\omega}(S^{(k)}|\theta^{(k)}) = P_{\nu}(\theta^{(k)})\prod_{x^{(l)} \in S^{(k)}} P_{\omega}(x^{(l)}|\theta^{(k)})$ , where  $\nu$  de-  
 321 notes the weights of the neural network responsible for sampling the parameters  $\theta^{(k)}$ , while  
 322  $\omega$  denotes the weights of the neural network responsible for sampling the bitstrings in the  
 323 batch  $S^{(k)}$ . The former, is an autoregressive NN that provides the parameters  $\mu$  and  $\kappa$  of a Von  
 324 Mises distribution [38] from which the basis-change parameters  $\theta^{(k)}$  are sampled. Due to the  
 325 autoregressive architecture,  $\mu_i$  and  $\kappa_i$  depend on the angles  $\theta_j$ , with  $j < i$ . The rotation angles  
 326  $\theta^{(k)}$  are also used as conditions for the other autoregressive NN that defines the probabilities  
 327  $P_{\omega}(x^{(l)}|\theta^{(k)})$  of each bitstrings  $x^{(l)}$ . The loss function to be minimized is defined as:

$$L = \sum_k \int d\theta^{(k)} \left[ P_{\nu}(\theta^{(k)}) \prod_{x^{(l)} \in S^{(k)}} P_{\omega}(x^{(l)}|\theta^{(k)}) \right]_{E^{(k)}} \quad (\text{E.1})$$

328 and its derivatives are

$$\begin{aligned}
\frac{\partial L}{\partial \omega} &= \sum_k \int d\theta^{(k)} \left[ P_{\nu}(\theta^{(k)}) \frac{\partial}{\partial \omega} \prod_{x^{(l)} \in S^{(k)}} P_{\omega}(x^{(l)} | \theta^{(k)}) \right] E^{(k)} \\
&= \sum_k \int d\theta^{(k)} \left[ P_{\nu}(\theta^{(k)}) P_{\omega}(S^{(k)} | \theta^{(k)}) \left( \sum_{x^{(l)} \in S^{(k)}} \frac{\partial \log(P_{\omega}(x^{(l)} | \theta^{(k)}))}{\partial \omega} \right) \right] E^{(k)} \\
&\simeq \frac{1}{K} \sum_{k=1}^K \left[ \sum_{x^{(l)} \in S^{(k)}} \frac{\partial \log(P_{\omega}(x^{(l)} | \theta^{(k)}))}{\partial \omega} \right] E^{(k)},
\end{aligned} \tag{E.2}$$

329 and

$$\begin{aligned}
\frac{\partial L}{\partial \nu} &= \sum_k \int d\theta^{(k)} \left[ \frac{\partial P_{\nu}(\theta^{(k)})}{\partial \nu} \prod_{x^{(l)} \in S^{(k)}} P_{\omega}(x^{(l)} | \theta^{(k)}) \right] E^{(k)} \\
&= \sum_k \int d\theta^{(k)} \left[ \frac{\partial P_{\nu}(\theta^{(k)})}{\partial \nu} \frac{P_{\nu}(\theta^{(k)})}{P_{\nu}(\theta^{(k)})} \prod_{x^{(l)} \in S^{(k)}} P_{\omega}(x^{(l)} | \theta^{(k)}) \right] E^{(k)} \\
&= \sum_k \int d\theta^{(k)} P_{\nu}(\theta^{(k)}) P_{\omega}(S^{(k)} | \theta^{(k)}) \left[ \frac{\partial \log(P_{\nu}(\theta^{(k)}))}{\partial \nu} \right] E^{(k)} \\
&\simeq \frac{1}{K} \sum_{k=1}^K \left[ \frac{\partial \log(P_{\nu}(\theta^{(k)}))}{\partial \nu} \right] E^{(k)},
\end{aligned} \tag{E.3}$$

330 where  $\omega \in \boldsymbol{\omega}$  and  $\nu \in \boldsymbol{\nu}$  denote single weights of the corresponding neural networks.

331 Therefore, including the baseline term, the loss is evaluated as:

$$L = \frac{1}{K} \sum_{k=1}^K \left[ \log(P_{\nu}(\theta^{(k)})) + \left( \sum_{x^{(l)} \in S^{(k)}} \log(P_{\omega}(x^{(l)} | \theta^{(k)})) \right) \right] (E^{(k)} - \overline{E^{(k)}}). \tag{E.4}$$

332 Sampling  $\theta^{(k)}$  from a conditional autoregressive NN is conceptually and practically appealing.  
333 Yet, the test results visualized in Fig. 9 indicate that this approach does not perform better  
334 than the gradient-based optimization described in Appendix B. The accuracy shows a similar  
335 improvement rate as a function of  $S$ , with an approximately constant upward shift, denoting  
336 a marginally worse performance.

## 337 F Problem of sampling unique configurations

338 As the size  $S$  of the configuration set increases, the probability of sampling already included  
339 configurations rapidly rises. This leads to a problematic computational cost for sampling  
340 unique configurations. To overcome this problem, we introduce the effective temperature  
341 parameter  $T$  [39]. This controls the shape of the output distribution by tuning the width of  
342 the softmax activation function in the final NN layer. The NN produces two outputs for each  
343 spin, and the softmax turns these outputs into probabilities of sampling 0 or 1. Specifically, if  
344  $Y_0$  and  $Y_1$  are the two outputs, then

$$\text{Softmax}(Y_q) = \frac{\exp(Y_q/T)}{\sum_{r \in \{0,1\}} \exp(Y_r/T)}. \tag{F.1}$$

345 Complementary strategies were introduced in Ref. [31]. During training, we set  $T = 1$ , but in  
346 the inference phase we increase  $T$  to have a broader distribution, thus favoring the sampling  
347 of different outputs. This effect is demonstrated in Fig. 10. Indeed, while with  $T = 1$  the

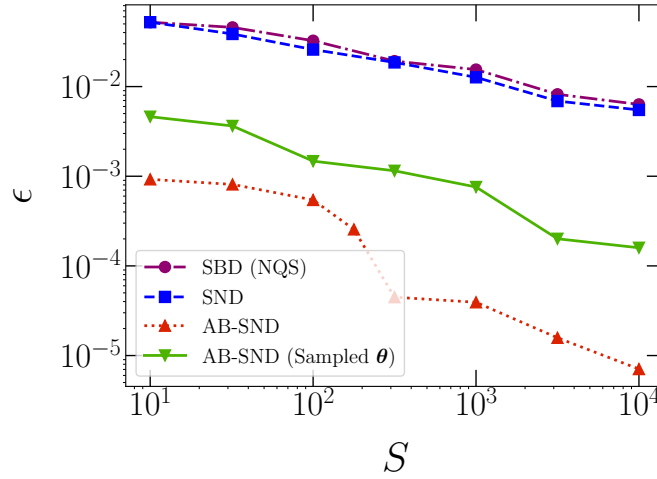


Figure 9: Relative error  $\epsilon$  as a function of the number of unique configurations  $S$  used to build the subspace Hamiltonian. These results are for the 1D-TFIM with  $h = 0.5$  and  $N = 50$ . We compare the accuracies of a standard SBD approach powered by NQS sampling, the SND approach, and two AB-SND approaches. The (green) upside-down triangles refer to the AB-SND approach with rotation parameters  $\theta^{(k)}$  sampled from an autoregressive NN, as explained in the text.

ratio between the number of unique configurations  $S$  and of total configurations  $N_s$  decreases almost exponentially fast, slightly larger effective temperatures suffice to significantly increase the number of unique configurations, thus drastically decreasing the computational cost of sampling.

Importantly, increasing  $T$  to values appropriate for efficient sampling does not reduce the performance of SND approaches. This is demonstrated in Fig. 11, where one observes that, for  $S \gtrsim 10^2$ , values of  $T \in [1, 1.6]$  provide comparable accuracies for the 1D-TFIM.

## G Autoregressive neural network and hyperparameters

We use a transformer encoder [40] with causal mask, two layers, four attention heads, and embedding size equal to 64. During training, we use  $K = 16$  batches for SND and  $K = 4$  batches for AB-SND, and number of sampled bitstrings equal to  $BS = 128$ . It is worth emphasizing that the latter does not coincide with the number of unique configurations  $S$  used during inference. Also, the rare repeated configurations are simply discarded. A comparison of the performances obtained with different values of  $K$  and  $BS$  is shown in Fig. 12. Notably, the accuracy of the SND method is not significantly affected by different choices for these parameters.



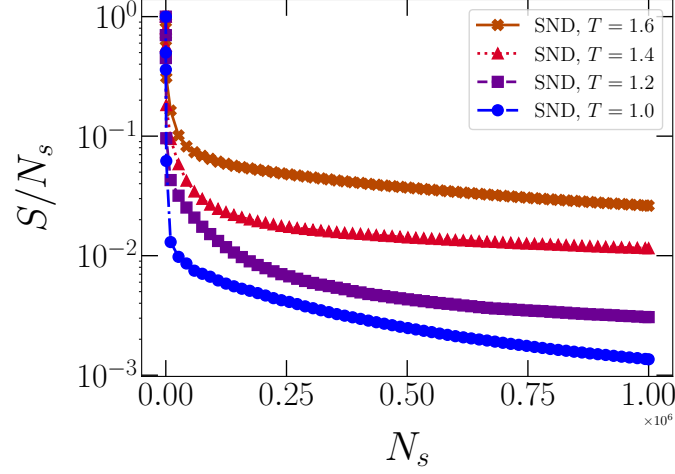


Figure 10: Ratio between number of unique configurations  $S$  and total number of samples  $N_s$  as a function of  $N_s$  for different values of the effective temperature  $T$ . The samples are obtained via SND for the 1D-TFIM with  $N = 50$  and  $h = 0.5$ .

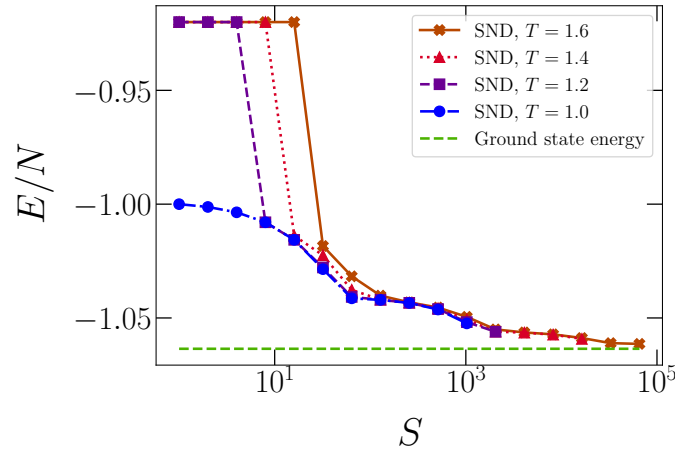


Figure 11: Energy per spin  $E/N$  obtained via SND as a function of the number of unique configurations  $S$  used to build the subspace Hamiltonian. The different datasets correspond to different effective temperatures  $T$ . The testbed model is the 1D-TFIM with  $N = 50$  spin and transverse field  $h = 0.5$ .

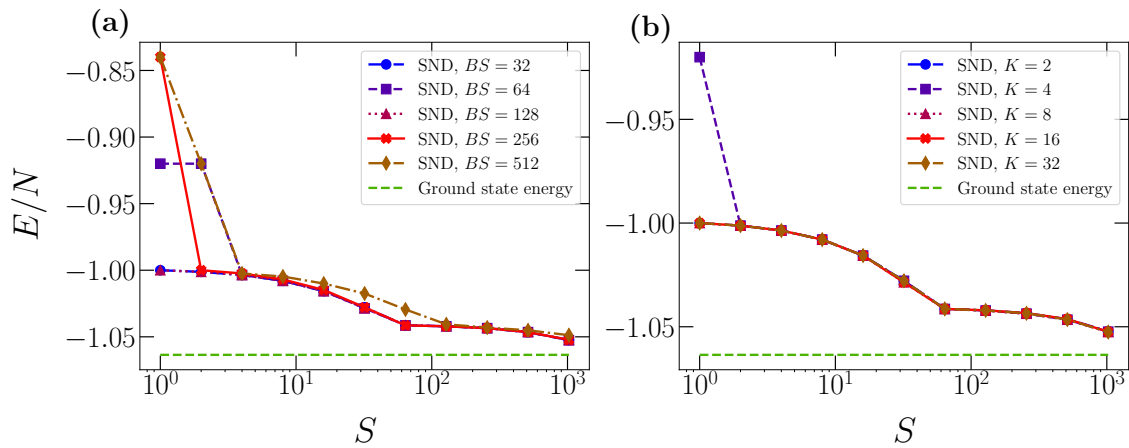


Figure 12: Energy per spin  $E/N$  obtained with SND as a function of the number of unique configurations  $S$  used to build the subspace Hamiltonian for the 1D-TFIM featuring  $N = 50$  spins and  $h = 0.5$ . Panels (a) and (b) display results for different values of  $BS$  and  $K$ , respectively.

## References

- [1] G. Carleo, I. Cirac, K. Cranmer, L. Daudet, M. Schuld, N. Tishby, L. Vogt-Maranto and L. Zdeborová, *Machine learning and the physical sciences*, Rev. Mod. Phys. **91**, 045002 (2019), doi:[10.1103/RevModPhys.91.045002](https://doi.org/10.1103/RevModPhys.91.045002).
- [2] J. Carrasquilla, *Machine learning for quantum matter*, Advances in Physics: X **5**(1), 1797528 (2020), doi:[10.1080/23746149.2020.1797528](https://doi.org/10.1080/23746149.2020.1797528).
- [3] H. J. Kulik, T. Hammerschmidt, J. Schmidt, S. Botti, M. A. L. Marques, M. Boley, M. Scheffler, M. Todorović, P. Rinke, C. Oses, A. Smolyanyuk, S. Curtarolo *et al.*, *Roadmap on machine learning in electronic structure*, Electronic Structure **4**(2), 023004 (2022), doi:[10.1088/2516-1075/ac572f](https://doi.org/10.1088/2516-1075/ac572f).
- [4] V. Dunjko and H. J. Briegel, *Machine learning & artificial intelligence in the quantum domain: a review of recent progress*, Reports on Progress in Physics **81**(7), 074001 (2018), doi:[10.1088/1361-6633/aab406](https://doi.org/10.1088/1361-6633/aab406).
- [5] N. Saraceni, S. Cantori and S. Pilati, *Scalable neural networks for the efficient learning of disordered quantum systems*, Phys. Rev. E **102**, 033301 (2020), doi:[10.1103/PhysRevE.102.033301](https://doi.org/10.1103/PhysRevE.102.033301).
- [6] K. Mills, K. Ryczko, I. Luchak, A. Domurad, C. Beeler and I. Tamblyn, *Extensive deep neural networks for transferring small scale learning to large scale systems*, Chem. Sci. **10**, 4129 (2019), doi:[10.1039/C8SC04578J](https://doi.org/10.1039/C8SC04578J).
- [7] F. A. Faber, L. Hutchison, B. Huang, J. Gilmer, S. S. Schoenholz, G. E. Dahl, O. Vinyals, S. Kearnes, P. F. Riley and O. A. von Lilienfeld, *Prediction errors of molecular machine learning models lower than hybrid DFT error*, Journal of Chemical Theory and Computation **13**(11), 5255 (2017), doi:[10.1021/acs.jctc.7b00577](https://doi.org/10.1021/acs.jctc.7b00577), PMID: 28926232.
- [8] G. Carleo and M. Troyer, *Solving the quantum many-body problem with artificial neural networks*, Science **355**(6325), 602–606 (2017), doi:[10.1126/science.aag2302](https://doi.org/10.1126/science.aag2302).

- [9] O. Sharir, Y. Levine, N. Wies, G. Carleo and A. Shashua, *Deep autoregressive models for the efficient variational simulation of many-body quantum systems*, Phys. Rev. Lett. **124**, 020503 (2020), doi:[10.1103/PhysRevLett.124.020503](https://doi.org/10.1103/PhysRevLett.124.020503).
- [10] T. D. Barrett, A. Malyshev and A. I. Lvovsky, *Autoregressive neural-network wavefunctions for ab initio quantum chemistry*, Nature Machine Intelligence **4**(4), 351 (2022), doi:[10.1038/s42256-022-00461-z](https://doi.org/10.1038/s42256-022-00461-z).
- [11] V. Abraham and N. J. Mayhall, *Selected configuration interaction in a basis of cluster state tensor products*, Journal of Chemical Theory and Computation **16**(10), 6098–6113 (2020), doi:[10.1021/acs.jctc.0c00141](https://doi.org/10.1021/acs.jctc.0c00141).
- [12] L. Craciunescu, A. W. Prentice and M. J. Paterson, *Selected configuration interaction for high accuracy and compact wave functions: Propane as a case study*, The Journal of Chemical Physics **162**(3), 034102 (2025), doi:[10.1063/5.0233542](https://doi.org/10.1063/5.0233542).
- [13] E. Giner, A. Scemama and M. Caffarel, *Using perturbatively selected configuration interaction in quantum Monte Carlo calculations*, Canadian Journal of Chemistry **91**(9), 879 (2013), doi:[10.1139/cjc-2013-0017](https://doi.org/10.1139/cjc-2013-0017).
- [14] T. Yanagisawa, *Quantum Monte Carlo diagonalization for many-fermion systems*, Phys. Rev. B **75**, 224503 (2007), doi:[10.1103/PhysRevB.75.224503](https://doi.org/10.1103/PhysRevB.75.224503).
- [15] J. Robledo-Moreno, M. Motta, H. Haas, A. Javadi-Abhari, P. Jurcevic, W. Kirby, S. Martiel, K. Sharma, S. Sharma, T. Shirakawa, I. Sitdikov, R.-Y. Sun *et al.*, *Chemistry beyond the scale of exact diagonalization on a quantum-centric supercomputer*, Science Advances **11**(25) (2025), doi:[10.1126/sciadv.adu9991](https://doi.org/10.1126/sciadv.adu9991).
- [16] N. Yoshioka, M. Amico, W. Kirby, P. Jurcevic, A. Dutt, B. Fuller, S. Garion, H. Haas, I. Hamamura, A. Ivrii, R. Majumdar, Z. Minev *et al.*, *Krylov diagonalization of large many-body hamiltonians on a quantum processor*, Nature Communications **16**(1) (2025), doi:[10.1038/s41467-025-59716-z](https://doi.org/10.1038/s41467-025-59716-z).
- [17] K. Kanno, M. Kohda, R. Imai, S. Koh, K. Mitarai, W. Mizukami and Y. O. Nakagawa, *Quantum-selected configuration interaction: Classical diagonalization of Hamiltonians in subspaces selected by quantum computers*, doi:<https://arxiv.org/abs/2302.11320>.
- [18] F. Arute, K. Arya, R. Babbush, D. Bacon, J. C. Bardin, R. Barends, R. Biswas, S. Boixo, F. G. Brandao, D. A. Buell *et al.*, *Quantum supremacy using a programmable superconducting processor*, Nature **574**(7779), 505 (2019), doi:<https://doi.org/10.1126/sciadv.adu9991>.
- [19] J. P. Coe, *Machine learning configuration interaction*, Journal of Chemical Theory and Computation **14**(11), 5739–5749 (2018), doi:[10.1021/acs.jctc.8b00849](https://doi.org/10.1021/acs.jctc.8b00849).
- [20] P. Bilous, L. Thirion, H. Menke, M. W. Haverkort, A. Pálffy and P. Hansmann, *Neural-network-supported basis optimizer for the configuration interaction problem in quantum many-body clusters: Feasibility study and numerical proof*, Phys. Rev. B **111**, 035124 (2025), doi:[10.1103/PhysRevB.111.035124](https://doi.org/10.1103/PhysRevB.111.035124).
- [21] P. Bilous, A. Pálffy and F. Marquardt, *Deep-learning approach for the atomic configuration interaction problem on large basis sets*, Phys. Rev. Lett. **131**, 133002 (2023), doi:[10.1103/PhysRevLett.131.133002](https://doi.org/10.1103/PhysRevLett.131.133002).

- [22] M. Rano and D. Ghosh, *Efficient machine learning configuration interaction for bond breaking problems*, The Journal of Physical Chemistry A **127**(16), 3705 (2023), doi:[10.1021/acs.jpca.2c09103](https://doi.org/10.1021/acs.jpca.2c09103).
- [23] J. Yu, J. R. Moreno, J. T. Iosue, L. Bertels, D. Claudino, B. Fuller, P. Groszkowski, T. S. Humble, P. Jurcevic, W. Kirby, T. A. Maier, M. Motta *et al.*, *Quantum-centric algorithm for sample-based Krylov diagonalization*, doi:<https://arxiv.org/abs/2501.09702>.
- [24] G. Carleo, K. Choo, D. Hofmann, J. E. T. Smith, T. Westerhout, F. Alet, E. J. Davis, S. Efthymiou, I. Glasser, S.-H. Lin, M. Mauri, G. Mazzola *et al.*, *Netket: A machine learning toolkit for many-body quantum systems*, SoftwareX p. 100311 (2019), doi:[10.1016/j.softx.2019.100311](https://doi.org/10.1016/j.softx.2019.100311).
- [25] F. Vicentini, D. Hofmann, A. Szabó, D. Wu, C. Roth, C. Giuliani, G. Pescia, J. Nys, V. Vargas-Calderón, N. Astrakhantsev and G. Carleo, *NetKet 3: Machine Learning Toolbox for Many-Body Quantum Systems*, SciPost Phys. Codebases p. 7 (2022), doi:[10.21468/SciPostPhysCodeb.7](https://doi.org/10.21468/SciPostPhysCodeb.7).
- [26] P. Pfeuty, *The one-dimensional Ising model with a transverse field*, Annals of Physics **57**(1), 79 (1970), doi:[https://doi.org/10.1016/0003-4916\(70\)90270-8](https://doi.org/10.1016/0003-4916(70)90270-8).
- [27] A. P. Young and H. Rieger, *Numerical study of the random transverse-field Ising spin chain*, Phys. Rev. B **53**, 8486 (1996), doi:[10.1103/PhysRevB.53.8486](https://doi.org/10.1103/PhysRevB.53.8486).
- [28] F. Becca and S. Sorella, *Quantum Monte Carlo approaches for correlated systems*, Cambridge University Press (2017).
- [29] L. Brodoloni and S. Pilati, *Zero-temperature Monte Carlo simulations of two-dimensional quantum spin glasses guided by neural network states*, Phys. Rev. E **110**, 065305 (2024), doi:[10.1103/PhysRevE.110.065305](https://doi.org/10.1103/PhysRevE.110.065305).
- [30] C.-Y. Park and M. J. Kastoryano, *Geometry of learning neural quantum states*, Phys. Rev. Res. **2**, 023232 (2020), doi:[10.1103/PhysRevResearch.2.023232](https://doi.org/10.1103/PhysRevResearch.2.023232).
- [31] P. Reinholdt, K. M. Ziemis, E. R. Kjellgren, S. Coriani, S. P. A. Sauer and J. Kongsted, *Fundamental limitations in sample-based quantum diagonalization methods*, doi:<https://arxiv.org/abs/2501.07231>.
- [32] W. W. Ho and T. H. Hsieh, *Efficient variational simulation of non-trivial quantum states*, SciPost Physics **6**(3) (2019), doi:[10.21468/scipostphys.6.3.029](https://doi.org/10.21468/scipostphys.6.3.029).
- [33] A. Asthana, A. Kumar, V. Abraham, H. Grimsley, Y. Zhang, L. Cincio, S. Tretiak, P. A. Dub, S. E. Economou, E. Barnes and N. J. Mayhall, *Quantum self-consistent equation-of-motion method for computing molecular excitation energies, ionization potentials, and electron affinities on a quantum computer*, Chem. Sci. **14**, 2405 (2023), doi:[10.1039/D2SC05371C](https://doi.org/10.1039/D2SC05371C).
- [34] S. Cantori, *Adaptive-basis sample-based neural diagonalization for quantum many-body systems*, GitHub repository, <https://github.com/simonecantori/Sample-based-Neural-Diagonalization>.
- [35] J. Li, X. Yang, X. Peng and C.-P. Sun, *Hybrid quantum-classical approach to quantum optimal control*, Phys. Rev. Lett. **118**, 150503 (2017), doi:[10.1103/PhysRevLett.118.150503](https://doi.org/10.1103/PhysRevLett.118.150503).
- [36] K. Mitarai, M. Negoro, M. Kitagawa and K. Fujii, *Quantum circuit learning*, Phys. Rev. A **98**, 032309 (2018), doi:[10.1103/PhysRevA.98.032309](https://doi.org/10.1103/PhysRevA.98.032309).

- 472 [37] A. Paszke, S. Gross, S. Chintala, G. Chanan, E. Yang, Z. DeVito, Z. Lin, A. Desmaison,  
473 L. Antiga and A. Lerer, *Automatic differentiation in pytorch*, In *NIPS-W* (2017).
- 474 [38] K. Mardia and P. Jupp, *Directional Statistics*, Wiley Series in Probability and Statistics. Wi-  
475 ley, ISBN 9780470317815 (2009), <https://books.google.it/books?id=PTNiCm4Q-M0C>.
- 476 [39] H. Xuan, B. Yang and X. Li, *Exploring the impact of temperature scaling in softmax for*  
477 *classification and adversarial robustness*, doi:<https://arxiv.org/abs/2502.20604>.
- 478 [40] A. Vaswani, N. Shazeer, N. Parmar, J. Uszkoreit, L. Jones, A. N. Gomez, L. Kaiser and  
479 I. Polosukhin, *Attention is all you need*, doi:<https://arxiv.org/abs/1706.03762>.